Supplementary Information for

Changing Arctic landscapes in a changing climate: thermokarst evolution in polygonal tundra

Ahmad Jan Khattak[1*] and Alexandra Hamm[2,3]

[1]NOAA Affiliate, Office of Water Prediction, National Water Center, Tuscaloosa, Alabama, USA
[2]Department of Physical Geography, Stockholm University, Stockholm, Sweden
[3]Bolin Centre for Climate Research, Stockholm University, Stockholm, Sweden

*Correspondence: Ahmad Jan Khattak
Email: ajkhattak@gmail.com; ahmad.jan@noaa.gov

Tables

Table S1. Study regions with corresponding latitude and longitude, mean annual air temperature (MAAT), mean annual ground temperature (MAGT), mean annual precipitation (MAP), and mean annual thaw depth (MATD). The sites are listed in the decreasing order of average MAGT and MAAT to illustrate the temperature gradient. This average takes into account the effect of snow as well, as MAGT is much greater than the MAAT due to the thermal effects of snow ---------- 3
Table S2. Parameters used in the dynamic subgrid model. Values for intermediate-centered polygons are linearly interpolated between low-centered polygons and high-centered polygons for subsidence values of 0 to 40 cm (see Fig. S14) ---------- 3
Table S3. Subsurface physical properties used in the study for the selected sites. S_{uf} and S_f refer to saturated unfrozen and frozen soil. Porosities for the excess-ice layer are presented in Table S4 and the literature/sources from where these values are extracted are provided in Table S6. ---------- 4
Table S4. Porosities at the top and bottom of the excess ice layer. Mean annual thaw depths (MATD) for all sites are provided in Table S1. Porosities are linearly interpolated between the top and bottom locations of the ice-wedge ---------- 5
Table S5. Overview of the literature. List of sources used in the study for the physical parameters, MAGT, and MATD ---------- 5
Table S6. Literature summary. List of sources of the observed meteorological data. Dash indicates observed data was unavailable ---------- 6

Figures

Figure S1. Evolution of the polygonal tundra landscapes, with initially undegraded state, under variations in the ground ice. (a) ice-poor landscapes, (b) ice-moderate landscapes, and (c) ice-rich landscapes. The colors indicate the state of the landscape: low-centered polygons (green), transitional polygons (yellow), and high-centered polygons (blue). Rows correspond to different sites. The polygon turnover time (yellow) decreases from top to bottom (colder to warmer permafrost conditions) and from left to right (ice-poor to ice-rich landscapes). 7
Figure S2. Historical meteorological data at the Fosheim Peninsula, Canada. Illustrations of annual averages: (a) precipitation, (b) air temperature, (c) relative humidity, (d) incoming shortwave radiations, and (e) wind speed. The colors represent observed (red), ERA5 (black), and ERA5 corrected data (green), with grey dashed horizontal lines indicating historical averages. 8
Figure S3. Historical meteorological data at the Samoylov Island, Siberia, Russia. Illustrations of annual averages: (a) precipitation, (b) air temperature, (c) relative humidity, (d) incoming shortwave radiations, and (e) wind speed. The colors represent observed (red), ERA5 (black), and ERA5 corrected data (green), with grey dashed horizontal lines indicating historical averages. Note that the observed data in (a) is the rain precipitation..... 9
Figure S4. Historical meteorological data at the Kolyma lowland tundra, Eastern Siberia, Russia. Illustrations of annual averages: (a) precipitation, (b) air temperature, (c) relative humidity, (d) incoming shortwave radiations, and (e) wind speed. The colors represent observed (red), ERA5 (black), and ERA5 corrected data (green), with grey dashed horizontal lines indicating historical averages. Note the relative

humidity and wind speed historical average (grey lines) are consistent with that of the Barrow and Samoylov sites. 10
Figure S5. Historical meteorological data at the Barrow, Northern Alaska. Illustrations of annual averages: (a) precipitation, (b) air temperature, (c) relative humidity, (d) incoming shortwave radiations, and (e) wind speed. The colors represent observed (red), ERA5 (black), and ERA5 corrected data (green), with grey dashed horizontal lines indicating historical averages. 11
Figure S6. Historical meteorological data at the Yamal Peninsula, Western Siberia, Russia. Illustrations of annual averages: (a) precipitation, (b) air temperature, (c) relative humidity, (d) incoming shortwave radiations, and (e) wind speed. The colors represent observed (red), ERA5 (black), and ERA5 corrected data (green), with grey dashed horizontal lines indicating historical averages. 12
Figure S7. Historical meteorological data at the Adventdalen, Svalbard, Norway. Illustrations of annual averages: (a) precipitation, (b) air temperature, (c) relative humidity, (d) incoming shortwave radiations, and (e) wind speed. The colors represent observed (red), ERA5 (black), and ERA5 corrected data (green), with grey dashed horizontal lines indicating historical averages. 13
Figure S8. Projected meteorological data at the Fosheim Peninsula, Canada. Illustrations of annual averages: (a) total precipitation, (b) rain precipitation, (c) snow precipitation, (d) air temperature, (e) incoming shortwave radiations, (f) relative humidity, and (g) wind speed. The colors represent observed historical (red), ERA5 (blue), and CESM data (green), with green dashed lines indicating projected CESM linear trends. 14
Figure S9. Projected meteorological data at the Samoylov Island, Siberia, Russia. Illustrations of annual averages: (a) total precipitation, (b) rain precipitation, (c) snow precipitation, (d) air temperature, (e) incoming shortwave radiations, (f) relative humidity, and (g) wind speed. The colors represent ERA5 (blue) and CESM data (green), with green dashed lines indicating projected CESM linear trends. 15
Figure S10. Projected meteorological data at the Kolyma lowland tundra, Eastern Siberia, Russia. Illustrations of annual averages: (a) total precipitation, (b) rain precipitation, (c) snow precipitation, (d) air temperature, (e) incoming shortwave radiations, (f) relative humidity, and (g) wind speed. The colors represent ERA5 (blue) and CESM data (green), with green dashed lines indicating projected CESM linear trends. 16
Figure S11. Projected meteorological data at the Barrow, Northern Alaska. Illustrations of annual averages: (a) total precipitation, (b) rain precipitation, (c) snow precipitation, (d) air temperature, (e) incoming shortwave radiations, (f) relative humidity, and (g) wind speed. The colors represent ERA5 (blue) and CESM data (green), with green dashed lines indicating projected CESM linear trends....17
Figure S12. Projected meteorological data at the Yamal Peninsula, Western Siberia, Russia. Illustrations of annual averages: (a) total precipitation, (b) rain precipitation, (c) snow precipitation, (d) air temperature, (e) incoming shortwave radiations, (f) relative humidity, and (g) wind speed. The colors represent ERA5 (blue) and CESM data (green), with green dashed lines indicating projected CESM linear trends. 18
Figure S13. Projected meteorological data at the Adventdalen, Svalbard, Norway. Illustrations of annual averages: (a) total precipitation, (b) rain precipitation, (c) snow precipitation, (d) air temperature, (e) incoming shortwave radiations, (f) relative humidity, and (g) wind speed. The colors represent ERA5 (blue) and CESM data (green), with green dashed lines indicating projected CESM linear trends. 19
Figure S14. Shown is the evolution of parameters in the dynamic subgrid model. Low-centered polygons, undegraded state, have not experienced any subsidence. Fully subsided polygons (high-centered polygons) have undergone a 40 cm subsidence. These values are consistent with those reported in Jan et al. (2018). 20

Table S1. Study regions with corresponding latitude and longitude, mean annual air temperature (MAAT), mean annual ground temperature (MAGT), mean annual precipitation (MAP), and mean annual thaw depth (MATD). The sites are listed in the decreasing order of average MAGT and MAAT to illustrate the temperature gradient. This average takes into account the effect of snow as well, as MAGT is much greater than the MAAT due to the thermal effects of snow

Site name	Study region	Latitude and longitude	MAAT (°C)	MAGT (°C)	(MAAT + MAGT)/2.0 (°C)	MAP (mm) (Total, rain, snow)	MATD (cm)
Fosheim peninsula	Eureka, Canada	(80°0'N, 84°30'W)	-16	-10	-13	100, 60, 40	60
Samoylov	Central Siberia, Russia	(72°22'N,126°28'E)	-12	-9	-10.5	200, 130, 70	50
Kolyma	Eastern Siberia, Russia	(68°55'N,161°30'E)	-11	-8	-9.5	205, 105, 100	85
Barrow	Northern Alaska (USA)	(71°17'N,156°47'W)	-11	-6	-8.5	380, 130, 250	35
Yamal Peninsula	Western Siberia (Russia)	(71°5'N, 66°57'E)	-6	-5	-5.5	390, 220, 170	110
Adventdalen	Svalbard (Norway)	(78°10'N, 16°15' E)	-4.7	-3	-3.8	275, 140, 135	100

Table S2. Parameters used in the dynamic subgrid model. Values for intermediate-centered polygons are linearly interpolated between low-centered polygons and high-centered polygons for subsidence values of 0 to 40 cm (see Fig. S14)

Subgrid parameters / Polygon type	Microtopographic relief (cm)	Soil excluded volume (cm)	Depression depth (cm)	Drag exponent (-)
Low-centered polygons	36.0	18.0	15.0	7.0
High-centered polygons	42.0	23.0	5.0	1.0

Table S3. Subsurface physical properties used in the study for the selected sites. S_{uf} and S_f refer to saturated unfrozen and frozen soil. Porosities for the excess-ice layer are presented in Table S4 and the literature/sources from where these values are extracted are provided in Table S6.

Soil layer / Parameter	Organic layer		Mineral layer		
	Barrow, Fosheim, Kolyma, Adventdalen*	**Yamal, Samoylov**	**Barrow, Fosheim, Kolyma**	**Yamal, Samoylov**	**Adventdalen**
Soil structure thickness	0.15 m	0.15 m	49.85 m	49.85 m	49.85
Porosity [-]	0.87	0.95	0.56	0.55	0.5
Intrinsic permeability [m^2]	9.38×10^{-12}	4.2×10^{-11}	6.0×10^{-13}	9.9×10^{-13}	10^{-12}
Residual saturation	0.0	0.0	0.2	0.2	0.0
van Genuchten alpha [Pa^{-1}]	5.1×10^{-4}	1.0×10^{-4} **	3.3×10^{-4}	6.3×10^{-4} **	8.0×10^{-4}
van Genuchten m [-]	1.9×10^{-1}	9.0×10^{-1}	2.48×10^{-1}	2.3×10^{-1}	2.0×10^{-1}
Thermal conductivity (S_{uf}) [W m^{-1} K^{-1}]	0.75	0.72	1.1	1.1*	1.7
Thermal conductivity (S_f)[W m^{-1} K^{-1}]	1.3	1.92	1.5	1.5*	1.5*
Thermal conductivity (dry) [W m^{-1} K^{-1}]	0.1	0.14	0.3	0.3*	0.27

*Jan, Coon, and Painter (2020)
**Ghanbarian-Alavijeh et al. (2010)

Table S4. Porosities at the top and bottom of the excess ice layer. Mean annual thaw depths (MATD) for all sites are provided in Table S1. Porosities are linearly interpolated between the top and bottom locations of the ice-wedge

Locations	Depth	Ice-poor	Ice-moderate	Ice-rich
Top of the ice-wedge	About 5 cm below the MATD	$\phi_{\text{mineral}} + 0.2$	$\phi_{\text{mineral}} + 0.25$	$\phi_{\text{mineral}} + 0.3$
Bottom of the ice-wedge	About 3 m below the current MATD	ϕ_{mineral}	ϕ_{mineral}	ϕ_{mineral}

Table S5. Overview of the literature. List of sources used in the study for the physical parameters, MAGT, and MATD

Site name	MAGT (°C)	MATD (cm)	Physical properties in the Table S4
Fosheim Peninsula	Pollard, Ward, and Becker (2015)	Nelson, Shiklomanov, and Nyland (2021)	Jan, Coon, and Painter (2020)
Samoylov	Boike et al. (2013); Liljedahl et al. (2016)	Nelson, Shiklomanov, and Nyland (2021); Boike et al. (2019)	Boike et al. (2019); (2013); Jan, Coon, and Painter (2020); Ghanbarian-Alavijeh et al. (2010)
Kolyma	Obu et al. (2020); Liljedahl et al. (2016)	Nelson, Shiklomanov, and Nyland (2021)	Jan, Coon, and Painter 2020
Barrow	Romanovsky, Smith, and Christiansen (2010); Liljedahl et al. (2016)	Nelson, Shiklomanov, and Nyland (2021)	Jan, Coon, and Painter 2020
Yamal Peninsula	Melnikov et al. (2022) http://gtnpdatabase.org/boreholes/view/1057	Nelson, Shiklomanov, and Nyland (2021)	Boike et al. (2019); (2013); Jan, Coon, and Painter (2020); Ghanbarian-Alavijeh et al. (2010)
Adventdalen	Hamm and Frampton (2021)	Nelson, Shiklomanov, and Nyland (2021)	Hamm and Frampton (2021); Tavakoli et al. (2021); Jan, Coon, and Painter (2020)

Table S6. Literature summary. List of sources of the observed meteorological data. Dash indicates observed data was unavailable

Site name	MAAT	MAP	RH	WS	ISWR
Fosheim Peninsula	https://climate.weather.gc.ca/ (station ID 1750)	https://climate.weather.gc.ca/ (station ID 1750)	(Lesins, Duck, and Drummond 2010)	(Lesins, Duck, and Drummond 2010)	-
Samoylov	(Boike et al. 2019b)	(Boike et al. 2019b)	(Boike et al. 2019b)	(Boike et al. 2019b)	(Boike et al. 2019b)
Kolyma	www.ncdc.noaa.gov (Station ID 251230)	(Veremeeva et al. 2021)	-	-	-
Barrow	Jan, Coon, and Painter (2019)	Jan, Coon, and Painter (2019)	Jan, Coon, and Painter (2019)	Jan, Coon, and Painter (2019)	Jan, Coon, and Painter (2019)
Yamal Peninsula	https://www2.gwu.edu/~calm/data/CALM_Data/Russia/West%20Siberia/r03_marre_sale/	https://www2.gwu.edu/~calm/data/CALM_Data/Russia/West%20Siberia/r03_marre_sale/	-	-	-
Adventdalen	https://www.unis.no/facilities/weather-stations/	https://www.unis.no/facilities/weather-stations/	https://www.unis.no/facilities/weather-stations/	https://www.unis.no/facilities/weather-stations/	https://www.unis.no/facilities/weather-stations/

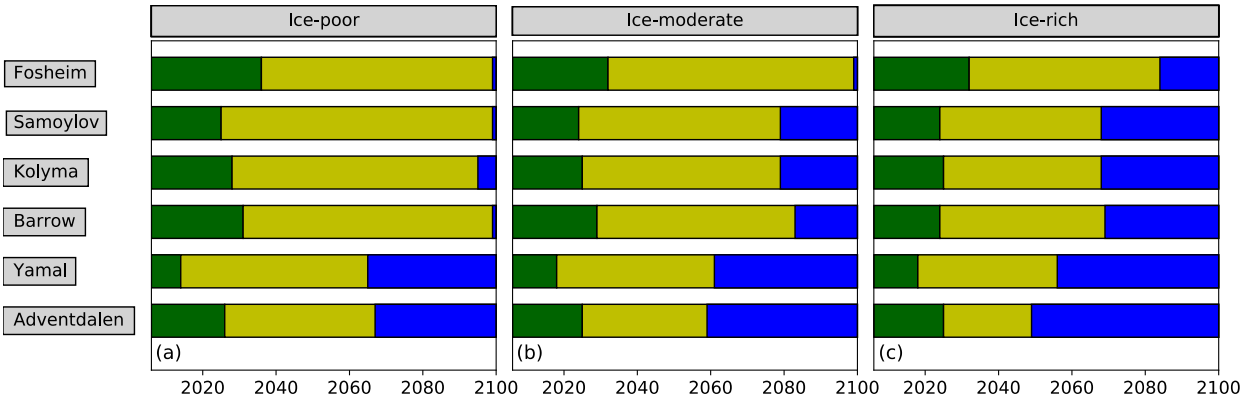

Figure S1. Evolution of the polygonal tundra landscapes, with initially undegraded state, under variations in the ground ice. (a) ice-poor landscapes, (b) ice-moderate landscapes, and (c) ice-rich landscapes. The colors indicate the state of the landscape: low-centered polygons (green), transitional polygons (yellow), and high-centered polygons (blue). Rows correspond to different sites. The polygon turnover time (yellow) decreases from top to bottom (colder to warmer permafrost conditions) and from left to right (ice-poor to ice-rich landscapes).

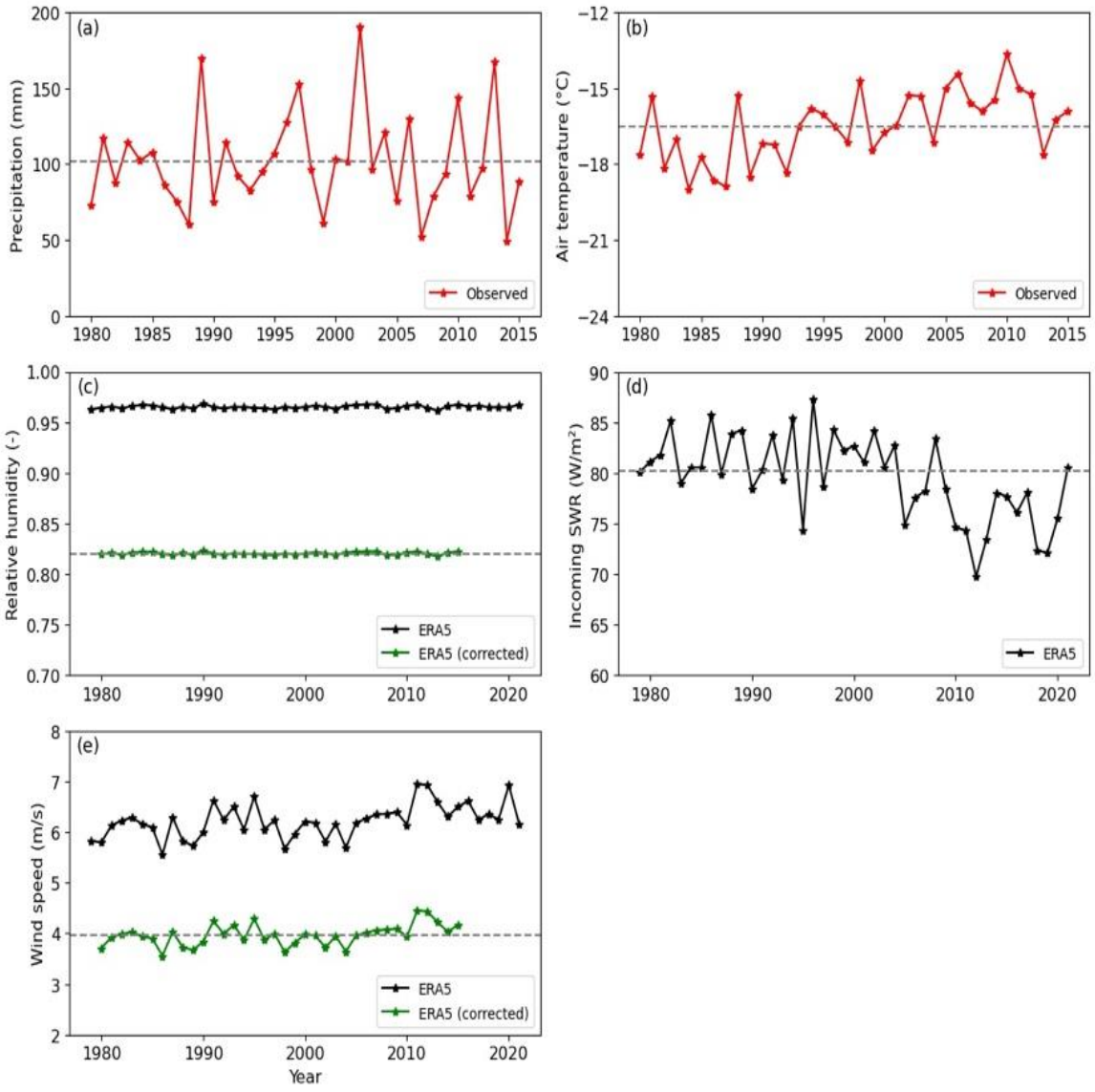

Figure S2. Historical meteorological data at the Fosheim Peninsula, Canada. Illustrations of annual averages: (a) precipitation, (b) air temperature, (c) relative humidity, (d) incoming shortwave radiations, and (e) wind speed. The colors represent observed (red), ERA5 (black), and ERA5 corrected data (green), with grey dashed horizontal lines indicating historical averages.

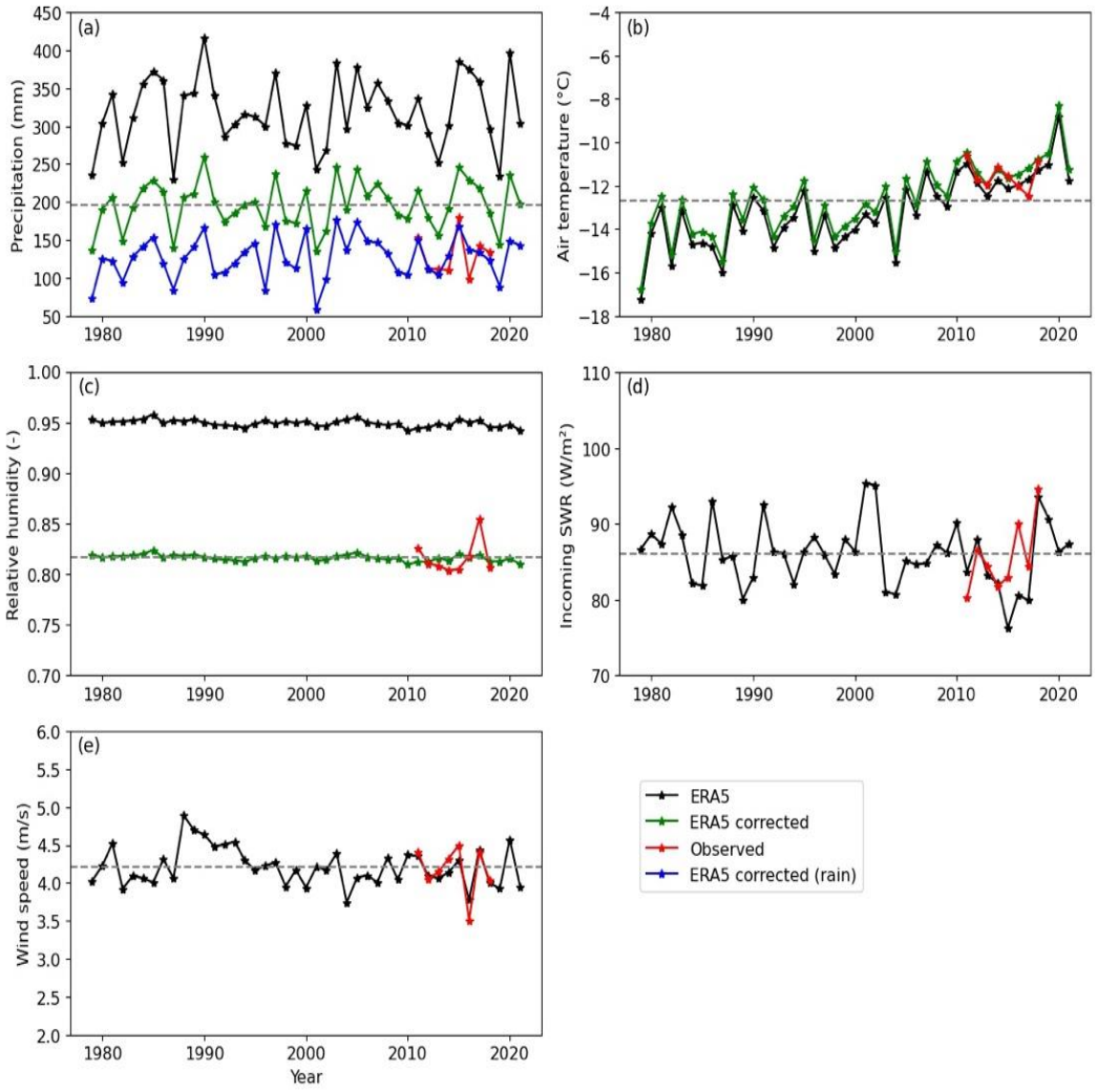

Figure S3. Historical meteorological data at the Samoylov Island, Siberia, Russia. Illustrations of annual averages: (a) precipitation, (b) air temperature, (c) relative humidity, (d) incoming shortwave radiations, and (e) wind speed. The colors represent observed (red), ERA5 (black), and ERA5 corrected data (green), with grey dashed horizontal lines indicating historical averages. Note that the observed data in (a) is the rain precipitation.

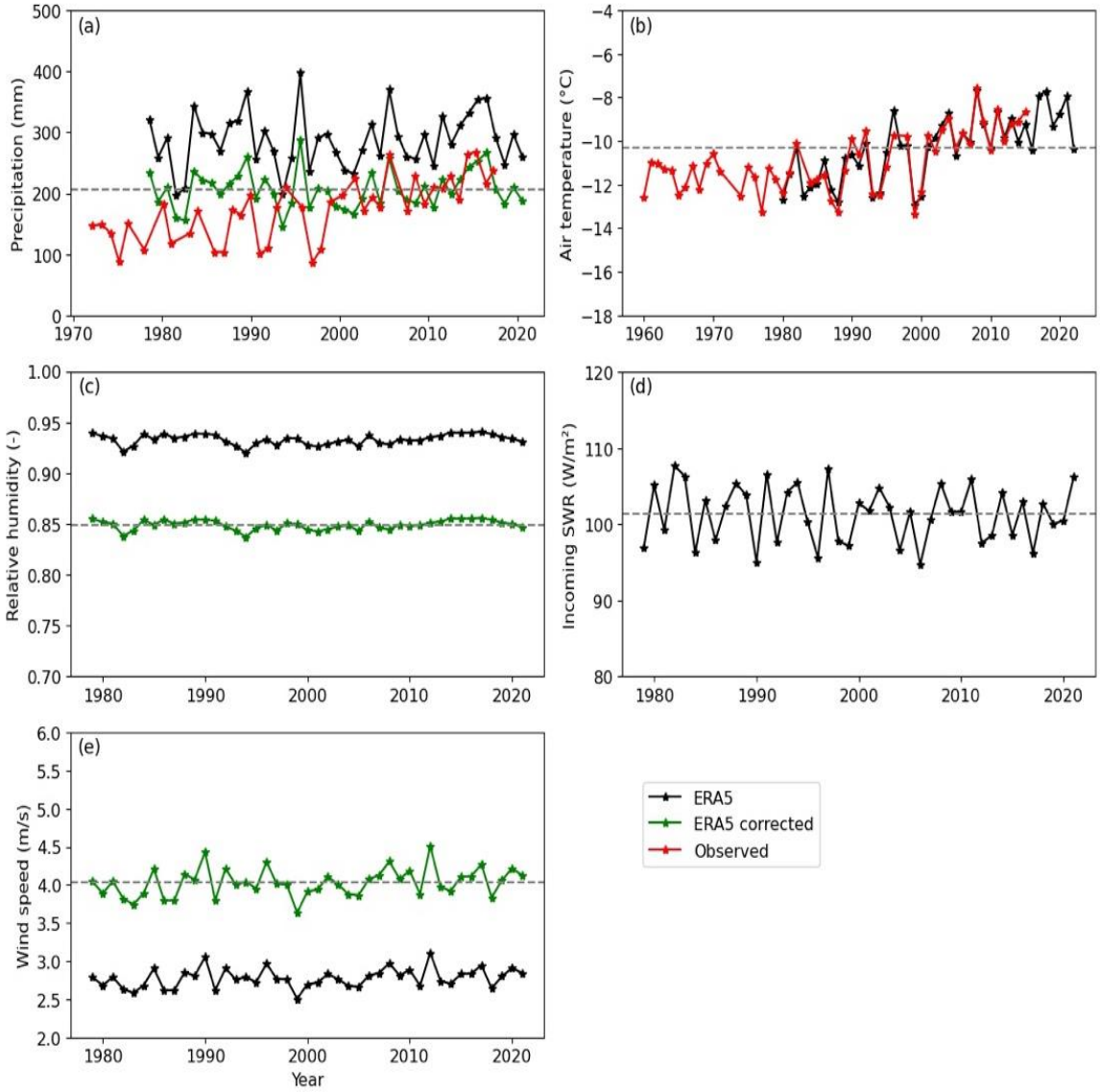

Figure S4. Historical meteorological data at the Kolyma lowland tundra, Eastern Siberia, Russia. Illustrations of annual averages: (a) precipitation, (b) air temperature, (c) relative humidity, (d) incoming shortwave radiations, and (e) wind speed. The colors represent observed (red), ERA5 (black), and ERA5 corrected data (green), with grey dashed horizontal lines indicating historical averages. Note the relative humidity and wind speed historical average (grey lines) are consistent with that of the Barrow and Samoylov sites.

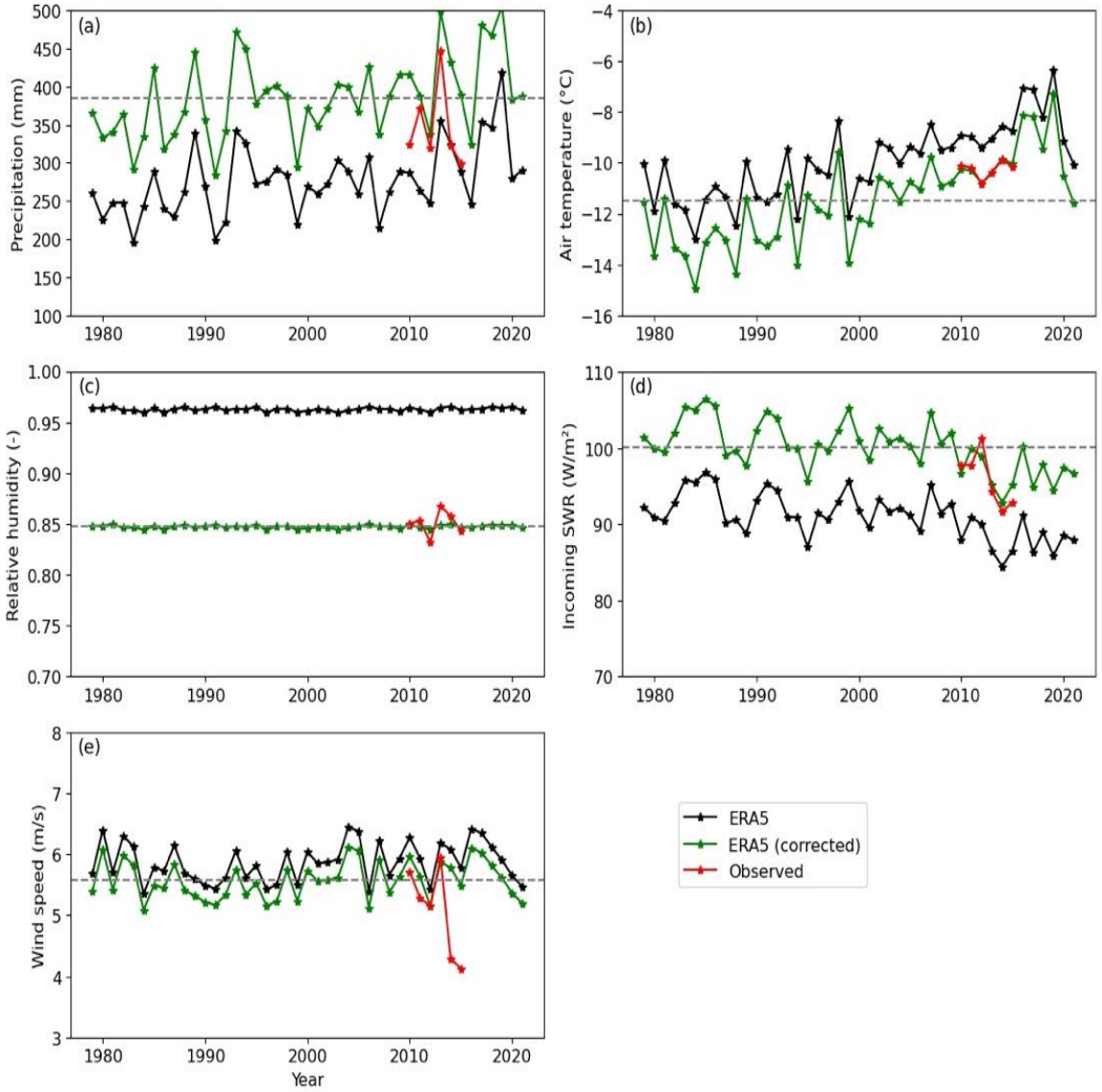

Figure S5. Historical meteorological data at the Barrow, Northern Alaska. Illustrations of annual averages: (a) precipitation, (b) air temperature, (c) relative humidity, (d) incoming shortwave radiations, and (e) wind speed. The colors represent observed (red), ERA5 (black), and ERA5 corrected data (green), with grey dashed horizontal lines indicating historical averages.

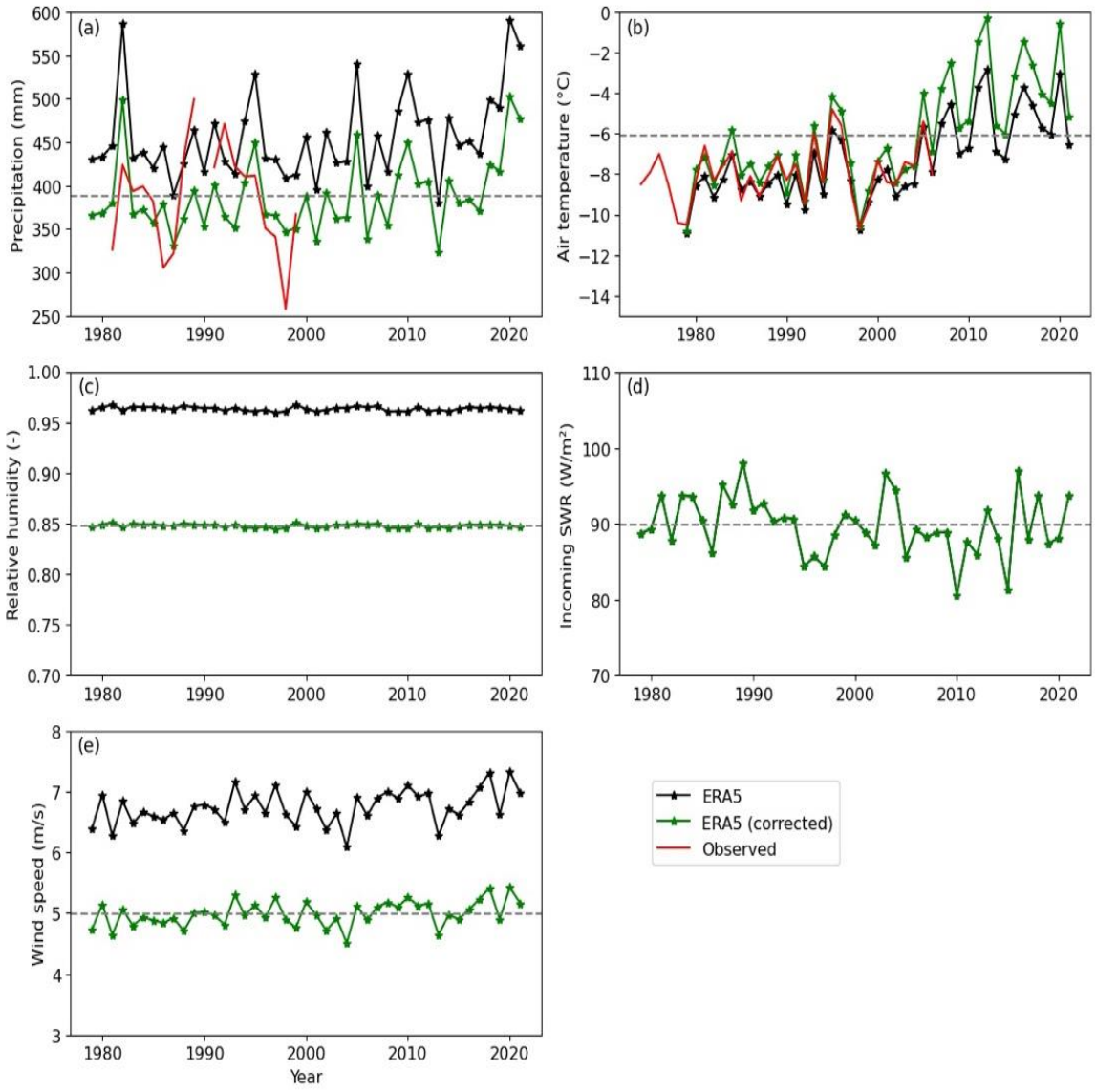

Figure S6. Historical meteorological data at the Yamal Peninsula, Western Siberia, Russia. Illustrations of annual averages: (a) precipitation, (b) air temperature, (c) relative humidity, (d) incoming shortwave radiations, and (e) wind speed. The colors represent observed (red), ERA5 (black), and ERA5 corrected data (green), with grey dashed horizontal lines indicating historical averages.

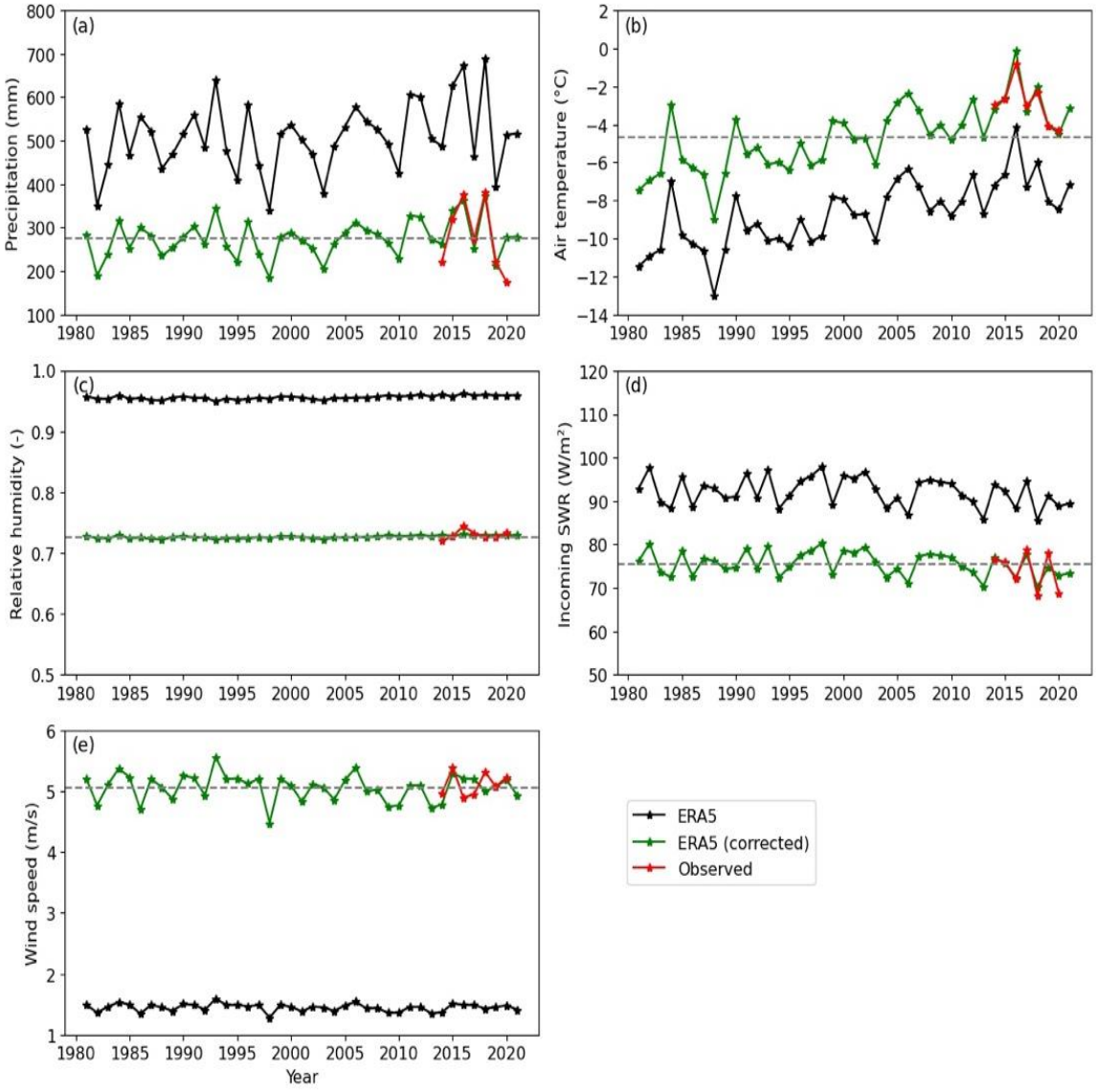

Figure S7. Historical meteorological data at the Adventdalen, Svalbard, Norway. Illustrations of annual averages: (a) precipitation, (b) air temperature, (c) relative humidity, (d) incoming shortwave radiations, and (e) wind speed. The colors represent observed (red), ERA5 (black), and ERA5 corrected data (green), with grey dashed horizontal lines indicating historical averages.

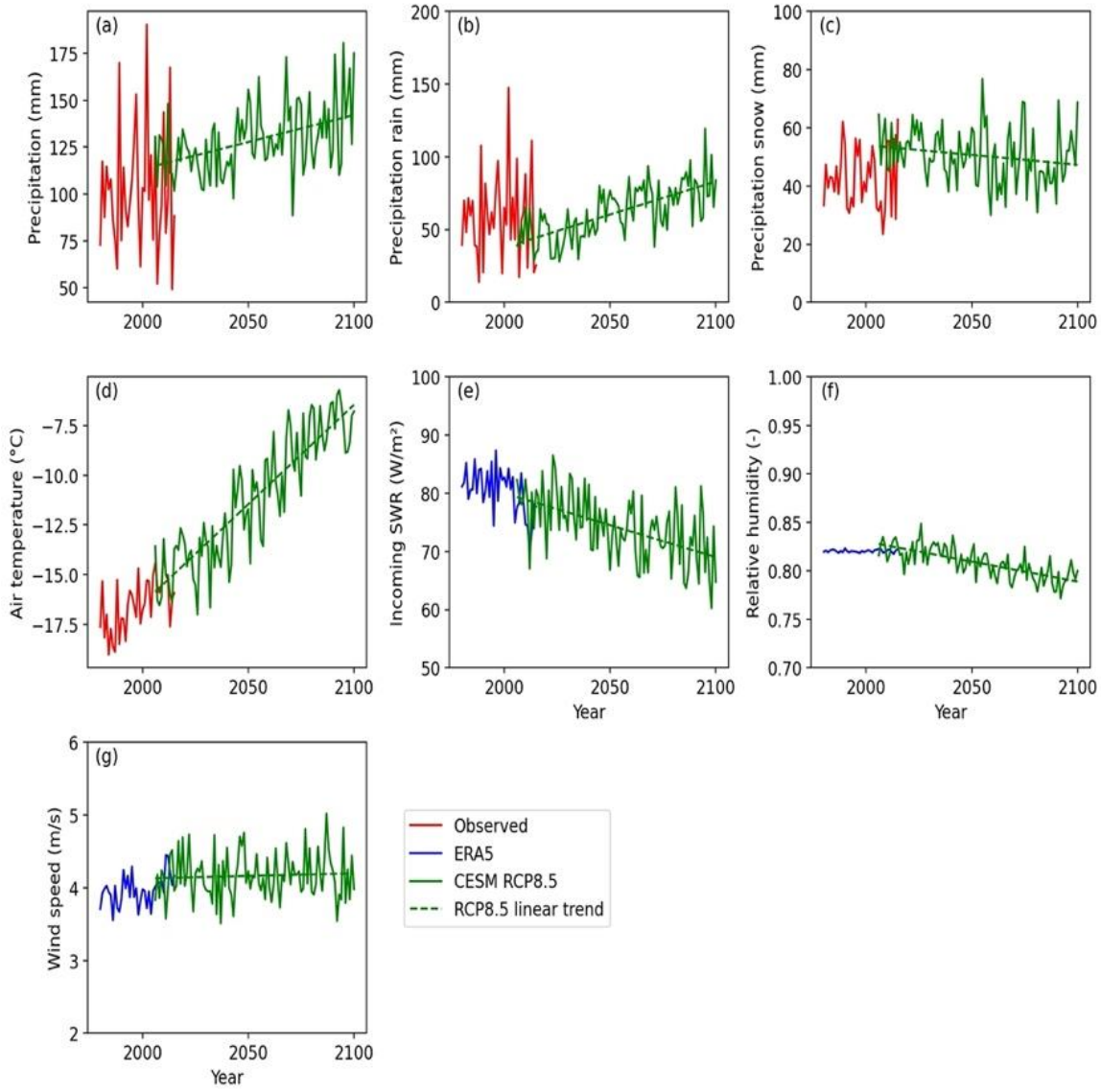

Figure S8. Projected meteorological data at the Fosheim Peninsula, Canada. Illustrations of annual averages: (a) total precipitation, (b) rain precipitation, (c) snow precipitation, (d) air temperature, (e) incoming shortwave radiations, (f) relative humidity, and (g) wind speed. The colors represent observed historical (red), ERA5 (blue), and CESM data (green), with green dashed lines indicating projected CESM linear trends.

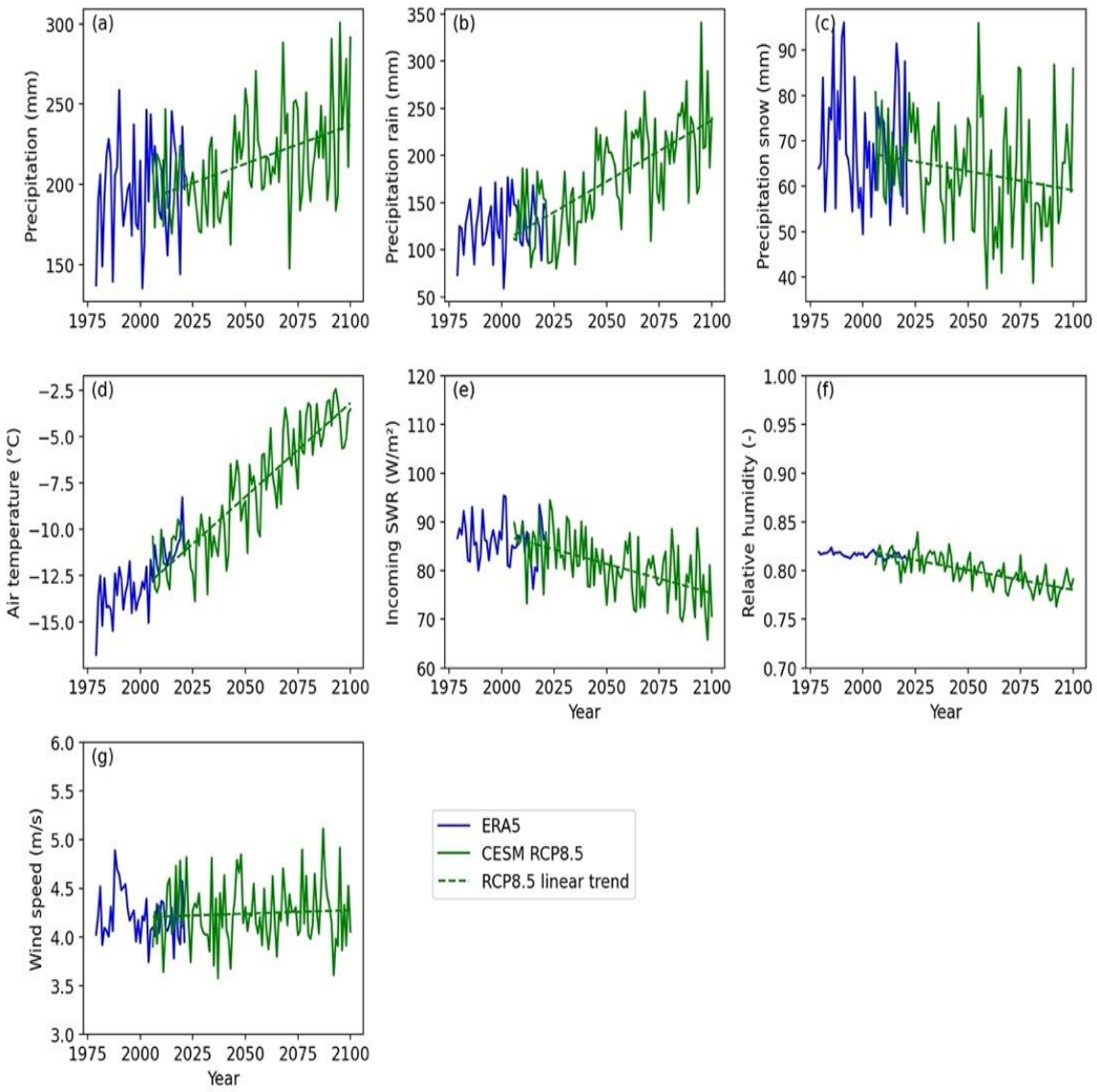

Figure S9. Projected meteorological data at the Samoylov Island, Siberia, Russia. Illustrations of annual averages: (a) total precipitation, (b) rain precipitation, (c) snow precipitation, (d) air temperature, (e) incoming shortwave radiations, (f) relative humidity, and (g) wind speed. The colors represent ERA5 (blue) and CESM data (green), with green dashed lines indicating projected CESM linear trends.

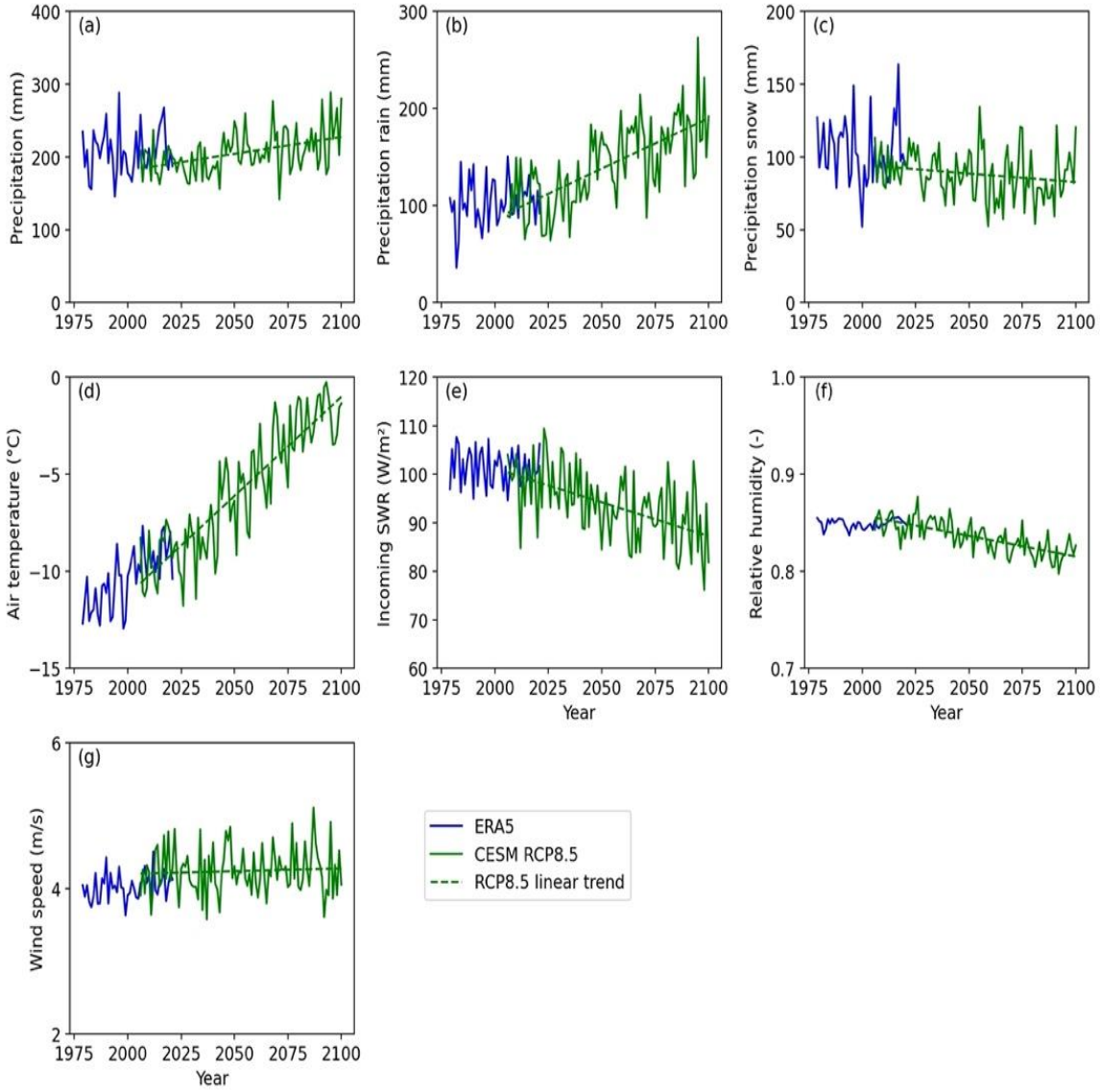

Figure S10. Projected meteorological data at the Kolyma lowland tundra, Eastern Siberia, Russia. Illustrations of annual averages: (a) total precipitation, (b) rain precipitation, (c) snow precipitation, (d) air temperature, (e) incoming shortwave radiations, (f) relative humidity, and (g) wind speed. The colors represent ERA5 (blue) and CESM data (green), with green dashed lines indicating projected CESM linear trends.

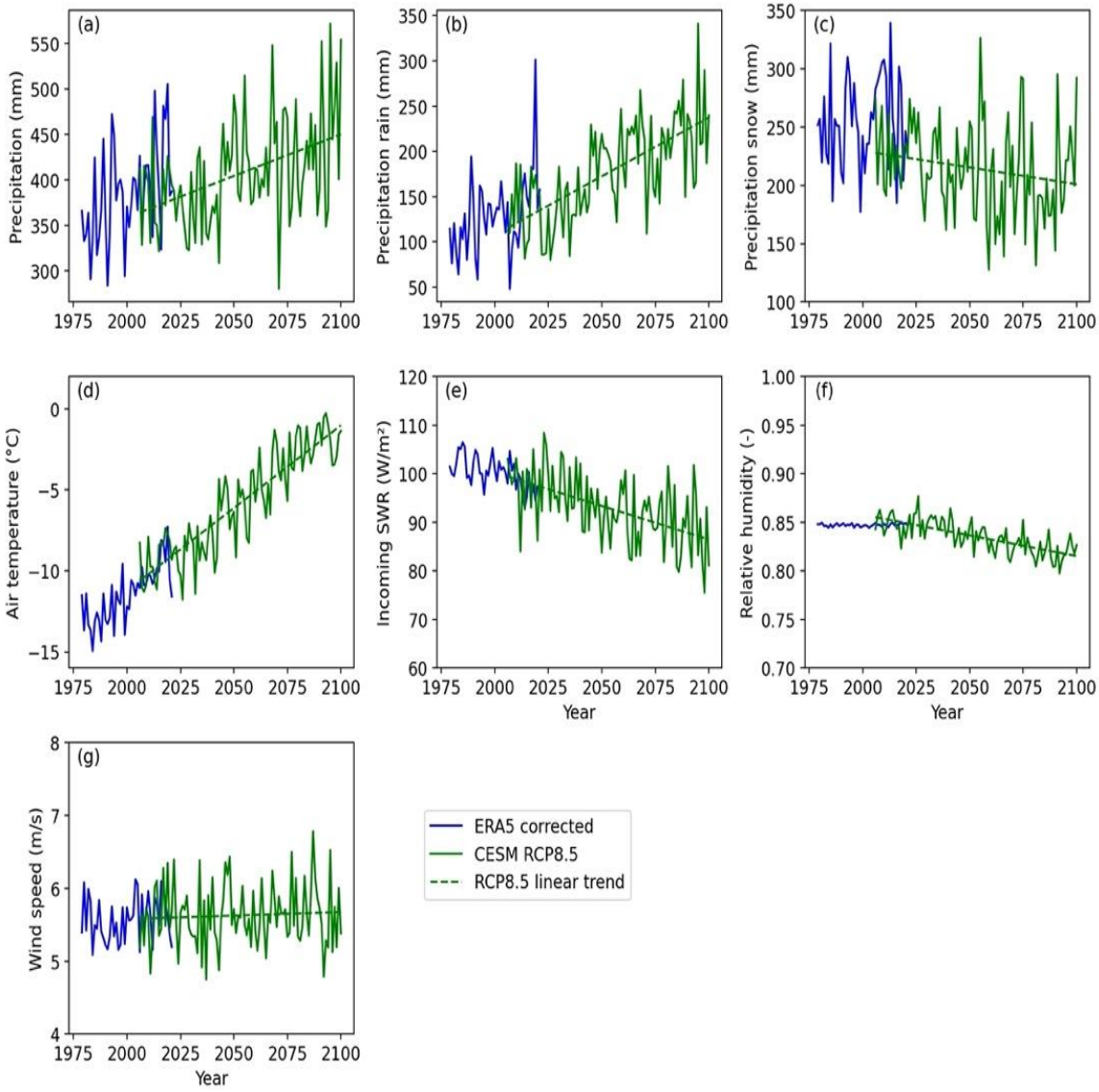

Figure S11. Projected meteorological data at the Barrow, Northern Alaska. Illustrations of annual averages: (a) total precipitation, (b) rain precipitation, (c) snow precipitation, (d) air temperature, (e) incoming shortwave radiations, (f) relative humidity, and (g) wind speed. The colors represent ERA5 (blue) and CESM data (green), with green dashed lines indicating projected CESM linear trends.

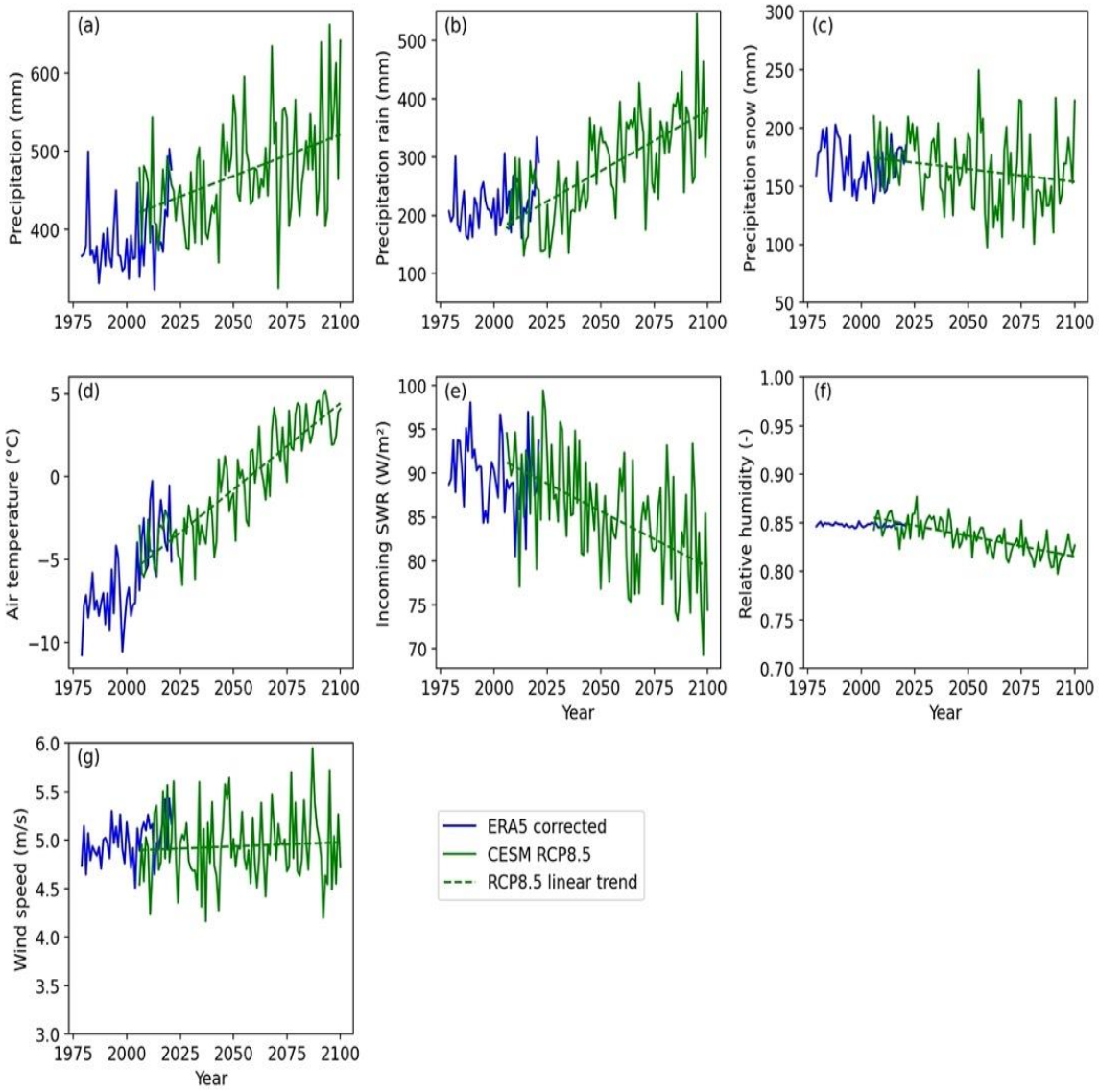

Figure S12. Projected meteorological data at the Yamal Peninsula, Western Siberia, Russia. Illustrations of annual averages: (a) total precipitation, (b) rain precipitation, (c) snow precipitation, (d) air temperature, (e) incoming shortwave radiations, (f) relative humidity, and (g) wind speed. The colors represent ERA5 (blue) and CESM data (green), with green dashed lines indicating projected CESM linear trends.

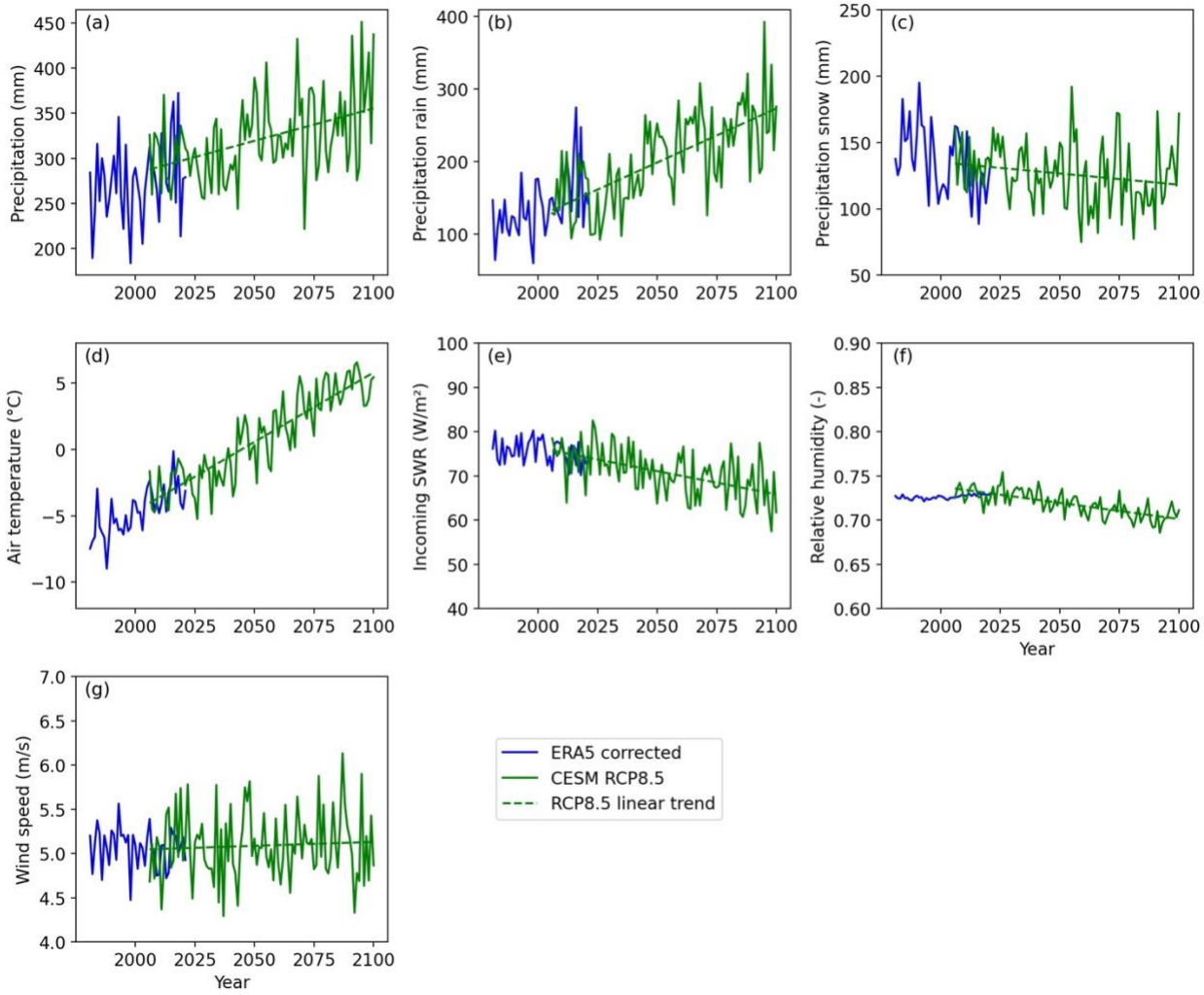

Figure S13. Projected meteorological data at the Adventdalen, Svalbard, Norway. Illustrations of annual averages: (a) total precipitation, (b) rain precipitation, (c) snow precipitation, (d) air temperature, (e) incoming shortwave radiations, (f) relative humidity, and (g) wind speed. The colors represent ERA5 (blue) and CESM data (green), with green dashed lines indicating projected CESM linear trends.

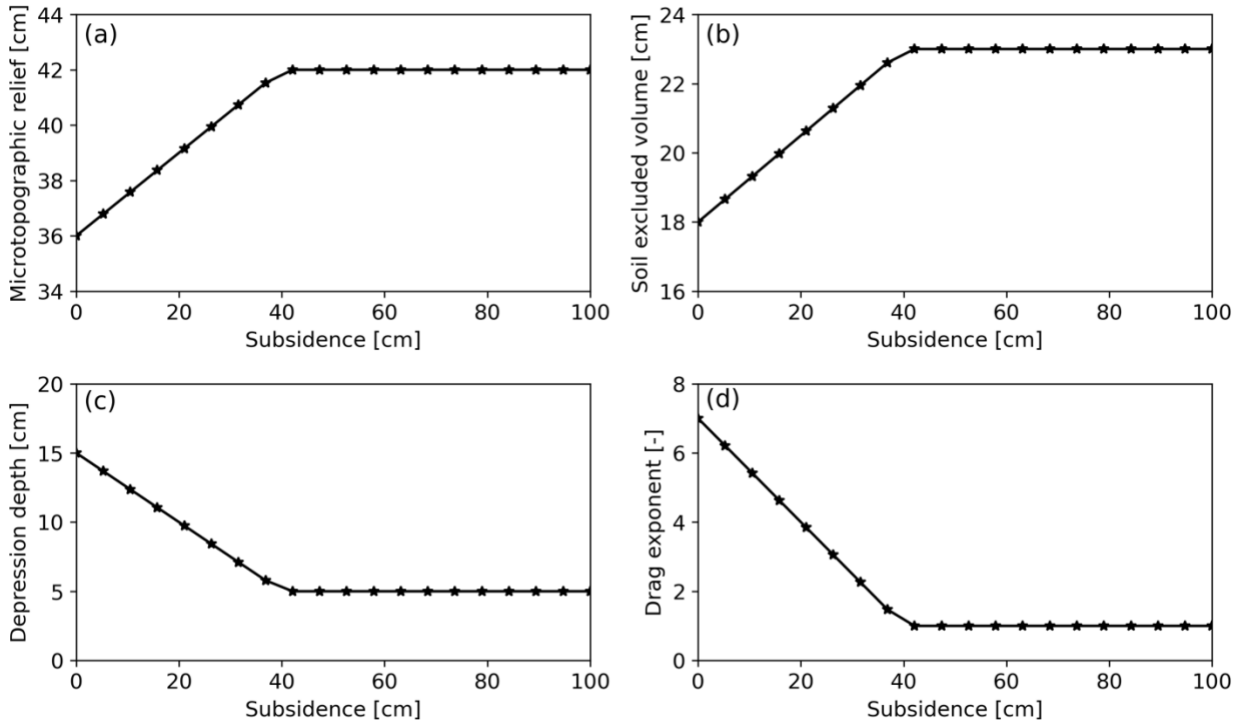

Figure S14. Shown is the evolution of parameters in the dynamic subgrid model. Low-centered polygons, undegraded state, have not experienced any subsidence. Fully subsided polygons (high-centered polygons) have undergone a 40 cm subsidence. These values are consistent with those reported in Jan et al. (2018).

Reference:

Boike, Julia, Britta Kattenstroth, Katya Abramova, Niko Bornemann, Antonina Chetverova, Irina Fedorova, Katrin Fröb, Mikhail Grigoriev, Maren Grüber, and Lars Kutzbach. 2013. "Baseline Characteristics of Climate, Permafrost and Land Cover from a New Permafrost Observatory in the Lena River Delta, Siberia (1998–2011)." *Biogeosciences* 10 (3): 2105–28.

Boike, Julia, Jan Nitzbon, Katharina Anders, Mikhail Grigoriev, Dmitry Bolshiyanov, Moritz Langer, Stephan Lange, Niko Bornemann, Anne Morgenstern, and Peter Schreiber. 2019a. "A 16-Year Record (2002–2017) of Permafrost, Active-Layer, and Meteorological Conditions at the Samoylov Island Arctic Permafrost Research Site, Lena River Delta, Northern Siberia: An Opportunity to Validate Remote-Sensing Data and Land Surface, Snow, and Permafrost Models." *Earth System Science Data* 11 (1): 261–99.

Boike, Julia, Jan Nitzbon, Katharina Anders, Mikhail N Grigoriev, Dimitry Yu Bolshiyanov, Moritz Langer, Stephan Lange, Niko Bornemann, Anne Morgenstern, and Peter Schreiber. 2019b. "Measurements in Soil and Air at Samoylov Station (2002-2018)." https://doi.pangaea.de/10.1594/PANGAEA.905232.

Ghanbarian-Alavijeh, B, A Liaghat, Guan-Hua Huang, and M Th Van Genuchten. 2010. "Estimation of the van Genuchten Soil Water Retention Properties from Soil Textural Data." *Pedosphere* 20 (4): 456–65.

Hamm, Alexandra, and Andrew Frampton. 2021. "Impact of Lateral Groundwater Flow on Hydrothermal Conditions of the Active Layer in a High-Arctic Hillslope Setting." *The Cryosphere* 15 (10): 4853–71. https://doi.org/10.5194/tc-15-4853-2021.

Jan, Ahmad, Ethan Coon, and Scott Painter. 2019. "Evaluating Integrated Surface/Subsurface Permafrost Thermal Hydrology Models in ATS (v0.88) Against Observations from a Polygonal Tundra Site:

Modeling Archive." Next Generation Ecosystems Experiment - Arctic, Oak Ridge National Laboratory (ORNL), Oak Ridge, TN (US); NGEE Arctic, Oak Ridge National Laboratory (ORNL), Oak Ridge, TN (United States). https://doi.org/10.5440/1545603.

Jan, Ahmad, Ethan T. Coon, Jake D. Graham, and Scott L. Painter. 2018. "A Subgrid Approach for Modeling Microtopography Effects on Overland Flow." *Water Resources Research* 54 (9): 6153–67. https://doi.org/10.1029/2017WR021898.

Jan, Ahmad, Ethan T. Coon, and Scott L. Painter. 2020. "Evaluating Integrated Surface/Subsurface Permafrost Thermal Hydrology Models in ATS (v0.88) against Observations from a Polygonal Tundra Site." *Geoscientific Model Development* 13 (5): 2259–76. https://doi.org/10.5194/gmd-13-2259-2020.

Lesins, G, TJ Duck, and JR Drummond. 2010. "Climate Trends at Eureka in the Canadian High Arctic." *Atmosphere-Ocean* 48 (2): 59–80.

Liljedahl, Anna K., Julia Boike, Ronald P. Daanen, Alexander N. Fedorov, Gerald V. Frost, Guido Grosse, Larry D. Hinzman, et al. 2016. "Pan-Arctic Ice-Wedge Degradation in Warming Permafrost and Its Influence on Tundra Hydrology." *Nature Geoscience* 9 (4): 312–18. https://doi.org/10.1038/ngeo2674.

Melnikov, Vladimir P, Victor I Osipov, Anatoli V Brouchkov, Svetlana V Badina, Marat R Sadurtdinov, Dmitry S Drozdov, Galina V Malkova, Mikhail N Zheleznyak, Oleg V Zhdaneev, and Nikolay A Ostarkov. 2022. "Past and Future of Permafrost Monitoring: Stability of Russian Energetic Infrastructure." *Energies* 15 (9): 3190.

Nelson, Frederick E, Nikolay I Shiklomanov, and Kelsey E Nyland. 2021. "Cool, CALM, Collected: The Circumpolar Active Layer Monitoring Program and Network." *Polar Geography* 44 (3): 155–66.

Obu, Jaroslav, Sebastian Westermann, Chloé Barboux, Annett Bartsch, Reynald Delaloye, Guido Grosse, Birgit Heim, et al. 2020. "ESA Permafrost Climate Change Initiative (Permafrost_cci): Permafrost Ground Temperature for the Northern Hemisphere, v2.0." Application/xml. Centre for Environmental Data Analysis (CEDA). https://doi.org/10.5285/6EBCB73158B14CD5A321B7C0BC6ED393.

Pollard, Wayne, Melissa Ward, and Michael Becker. 2015. "The Eureka Sound Lowlands: An Ice-Rich Permafrost Landscape in Transition." *Proceedings of GeoQuebec*.

Romanovsky, Vladimir E., Sharon L. Smith, and Hanne H. Christiansen. 2010. "Permafrost Thermal State in the Polar Northern Hemisphere during the International Polar Year 2007–2009: A Synthesis." *Permafrost and Periglacial Processes* 21 (2): 106–16.

Tavakoli, Saman, Graham Gilbert, Asgeir Olaf Kydland Lysdahl, Regula Frauenfelder, and Cathinka Schaanning Forsberg. 2021. "Geoelectrical Properties of Saline Permafrost Soil in the Adventdalen Valley of Svalbard (Norway), Constrained with in-Situ Well Data." *Journal of Applied Geophysics* 195: 104497.

Veremeeva, Alexandra, Ingmar Nitze, Frank Günther, Guido Grosse, and Elizaveta Rivkina. 2021. "Geomorphological and Climatic Drivers of Thermokarst Lake Area Increase Trend (1999–2018) in the Kolyma Lowland Yedoma Region, North-Eastern Siberia." *Remote Sensing* 13 (2): 178.